ISSN 0021-3640, JETP Letters, 2026, Vol. 123, No. 3, pp. 158–166. © Pleiades Publishing, Ltd., 2026.
Russian Text © The Author(s), 2026, published in Pis'ma v Zhurnal Eksperimental'noi i Teoreticheskoi Fiziki, 2026, Vol. 123, No. 3, pp. 177–186.

OPTICS
AND LASER PHYSICS

Simulation of Brillouin Oscillations Generated by a Metamaterial Based on a Nanostructured Nickel Film

A. V. Dyshlyuk[a,b], S. A. Romashevskiy[c], Yu. V. Petrov[d,e], V. A. Khokhlov[d], O. B. Vitrik[a], and N. A. Inogamov[d,f,c,*]

[a] *Institute of Automation and Control Processes, Far Eastern Branch, Russian Academy of Sciences, Vladivostok, 690041 Russia*
[b] *Vladivostok State University, Vladivostok, 690014 Russia*
[c] *Joint Institute for High Temperatures, Russian Academy of Sciences, Moscow, 125412 Russia*
[d] *Landau Institute for Theoretical Physics, Russian Academy of Sciences, Chernogolovka, Moscow region, 142432 Russia*
[e] *Moscow Institute of Physics and Technology (National Research University), Dolgoprudny, Moscow region, 141701 Russia*
[f] *Dukhov Automatics Research Institute, State Atomic Energy Corporation ROSATOM, Moscow, 127030 Russia*
**e-mail: nailinogamov@gmail.com*

Received November 5, 2025; revised December 10, 2025; accepted December 12, 2025

Brillouin oscillations associated with the reflection of light from a traveling acoustic wave in glass have been analyzed theoretically and experimentally. An ultrahigh-frequency acoustic wave is generated by irradiating a metasurface with a femtosecond laser pulse, which is a nanostructured optically thick (6–7 skin layers) nickel film on a glass substrate. The metasurface is a disordered ensemble of subwavelength spherical nanoantennas embedded in a film with a hollow gap. By significantly increasing the transmittance of the metafilm, nanoantennas make it possible to observe Brillouin oscillations through it. For the first time to the best of our knowledge, the phase of Brillouin oscillations generated by the metamaterial has been correctly determined by hybrid hydrodynamic and electrodynamic numerical simulation, and the relationship between the phase of Brillouin oscillations and the morphology of the metafilm has been established. This work is at the intersection of nanophotonics, plasmonics, and optoacoustics and is of interest to a wide range of specialists due to the prospects for using the described effects in active metadevices and highly sensitive sensors.

DOI: 10.1134/S0021364025610553

1. INTRODUCTION, GENERAL PICTURE

Metasurfaces are artificially created materials with pre-programmed desired optical properties [1–5]. They use ensembles of individual subwavelength nanostructured elements (meta-atoms/nanoantennas) [3]. By changing the ensemble and/or its meta-atoms, one can control the amplitude, polarization, and phase of the spectra of reflected and transmitted light (spectral deformations) [1–3]. These are the technologies of nanophotonics [2, 3, 5] and sensorics [3, 4, 6]. The enhancement of Raman scattering and luminescence in the near electromagnetic field is used in sensors.

In our case, meta-atoms are randomly distributed spherical inclusions, deeply embedded in the film and surrounded by thin gaps [7]. This is the difference from a large group of previous works, where the ordered arrays of nanoparticles, located either above or on the surface, were used. Note that disordered subwavelength metamaterials also form a large group, see the extensive detailed review [8]. They include natural objects (for example, structures on a butterfly's wing [8]), as well as artificially created structures with various degrees of order, see [8].

Artificial random micro- and nanostructures are known to occur after the ultrashort laser irradiation due to melting, foaming, and crystallization of the membranes of destroyed foams [9, 10]. They can also be attributed to artificial disordered metamaterials, since they are associated with strong spectral deformations, for example, blackening [11–13], i.e., a sharp change in the reflection spectrum. Meanwhile, these works went unnoticed by the authors of the review [8].

The spatial structure of our metamaterial was analyzed in [7]. The inclusions work as dipole nanoantennas. The concentration of the electromagnetic energy in gaps and its increase have been studied using numerical simulation of the electrodynamic problem in recent works [7, 14]. The gaps act as conductors of the electromagnetic field through the film into the glass substrate. Meanwhile, the reflection and transmission spectra from our metafilm are deformed.

Another extremely popular field of research and application is optoacoustics, where it is used to diagnose the internal state of a sample at depths of up to a

few microns [15, 16], similar to medical ultrasound practice. In this sense, optoacoustics supplements scanning electron and atomic force microscopy study of the surface with the analysis of subsurface layers.

Internal optical, elastic [15, 16], and even diffusion (in relation to the transport of heat and atoms) [17] characteristics are determined. To generate an acoustic wave, an optoacoustic transducer in the form of an ultrathin metal film is used [15, 16, 18]. The film is irradiated with a femtosecond laser pulse [7]. Due to thermal expansion caused by the absorption of the laser energy, the acoustic wave is generated in the film. This wave is emitted from the nickel film into the underlying substrate [7, 15, 16, 18], see the text below and Figs. 1 and 2.

The device discussed here combines nanophotonics (ensemble of nanoantennas) and optoacoustics into an interconnected optoacoustic metamaterial. This combination of areas of research is described in [7], where optical characteristics indicating spectral deformations, which proved the fabrication of a metamaterial. In particular, the transmittance is high (transparency). Due to the transparency of the metafilm, resonances, which we call Brillouin oscillations (BOs), are optically detected through it. In [7], these resonances were detected experimentally.

Let us explain the meaning of this work in comparison with [7]. In Section 6 of this work, BOs (see Fig. 1) are *quantitatively* attributed *for the first time* to the reflection of probe light from the acoustic wave traveling in glass by means of the numerical simulation. It is shown that calculated BOs of the reflection coefficient are in agreement with experimental data. The simulation reported in this work is based on a novel approach combining hydrodynamics and electrodynamics.

This is the fundamental difference of this work from the recent previous work [7]. In [7], electrodynamics was in no way related to hydrodynamics, which was responsible for the absorption of light, heating, and forming and emitting sound, and was used only to calculate spectral deformations (extraordinary transmittance). Thus, using electrodynamics, it was proved in [7] that our film can be classified as a metamaterial. The detailed electrodynamic calculation in [7] was based on the specific morphology of dipole nanoantennas (gaped balls) revealed in [7] using a focused ion beam and a scanning electron microscope.

2. ACOUSTIC PART

Figure 1 shows laser-induced changes in the relative reflectance $\Delta R(t)/R_0$ at a wavelength of 793 nm. Measurements were made in a pump–probe optical scheme using an extremely sensitive lock-in detection of the reflected signal. We studied a nickel metafilm sample on a glass substrate. The absorbed energy density of a pump pulse was 10.9 mJ/cm^2. The pump and

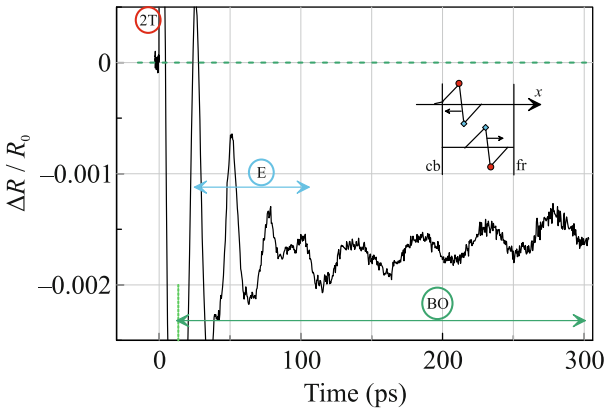

Fig. 1. (Color online) Time dependence of the correction $\Delta R(t)/R_0$ to the unperturbed reflection coefficient (i.e., before the arrival of the pump pulse) referring to the zero level shown by the green dashed horizontal straight line. In the first time interval (2T), the reflection is determined by the two-temperature (2T) state with $T_e \gg T_i$ of the nickel skin layer. The 2T relaxation in nickel is completed in about 1 ps [7, 19]. The transition to the 2T stage is usually accompanied by an increase in the reflection coefficient in poorly reflecting metals and by a decrease in it in well-reflecting metals (Au, Ag). In the second time interval (E), echo from acoustic waves in nickel reflected from the interface with the glass prevails. The third time interval (BO) is the region of Brillouin oscillations.

probe femtosecond laser pulses were incident on the sample from the side of the optoacoustic transducer, i.e., through the front edge fr of the film in the inset of Fig. 1.

As shown in the inset of Fig. 1, the pump laser pulse is incident on the right and is absorbed in the skin layer near the front edge fr of the film. The film with the thickness $d_f = 70$ nm is located between the planes fr and cb (see Fig. 1, inset), where cb is the contact boundary between the nickel and the glass substrate, which is located to the left of the plane cb. The x axis is perpendicular to the film plane and is direct against the laser beam.

As a result of the absorption of the energy of the pump laser pulse, the acoustic wave is formed in the nickel film. In the inset of Fig. 1, the density profile in this wave is shown as an upper zigzag with a red circle on the top. The width of each of the two zigzag triangles is determined by the heating depth $d_T \approx 25$ nm in the nickel. The heating layer in nickel is thicker than the skin layer; i.e., $d_T > d_{sk} = 11-12$ nm. After exposure, the wave propagates from right to left in the direction of the cb contact, see the left arrow in the inset of Fig. 1.

In a narrow (compared to the duration of the zigzag) time interval with a width of 1.7 ps, the region of the abrupt change of the pressure sign passes through the contact cb into the glass. In the inset of Fig. 1, the time interval of the change of the sign is located

between the red circle and the blue diamond on the zigzags. This interval is marked in Fig. 1 with the green dotted vertical straight line at the time ≈13 ps. Formally, it begins the region of BOs indicated as BO and marked by a green double-sided arrow in Fig. 1. The right end of the arrow at $t \approx 300$ ps is determined by the duration of the probe data collection in our experiment.

In the linear acoustic approximation, the upper zigzag running to the left in the inset of Fig. 1 passes into the glass with the unchanged shape and the amplitude of about one third of the amplitude of the incident wave (red circle on the upper zigzag); i.e., $T_{ac} = 2z_s/(z_s + z_f) \approx 1/3$, where z_s and z_f are the acoustic impedances of the glass substrate and nickel film, respectively. The wave reflected from the contact cb is shown by the lower zigzag running to the right (in the direction indicated by the arrow) in the inset of Fig. 1. The reflection is accompanied by a decrease in the amplitude and the reversal of the wave propagation direction; the reflection coefficient from the contact cb is $R_{ac} = (z_s - z_f)/(z_s + z_f) \approx 0.7$.

If the reflection coefficient of the wave in nickel from the front edge fr contacting with air is equal to unity, the coefficient R_{ac} is the common ratio of the geometric sequence in the sequence of bursts, which is represented by the acoustic wave in the glass. The acoustic pattern is considered in [7, 19], where echo in the film was analyzed (stage E in Fig. 1). This work is aimed at the theoretical analysis of the BO stage (the section BO in Fig. 1). Such an analysis is added to the scientific discourse for the first time. The successive bursts of the wave in the glass are separated by a time interval of about 26–27 ps, which is necessary for the passage of the zigzag from the time of reflection from the boundary cb, reflection from the edge fr, and return to the contact cb (one round pass in the film).

The acoustic echo region in the film (E in Fig. 1) begins with an increase in the density in the skin layer due to the arrival of a compression wave in the skin layer (the blue diamond on the lower zigzag in the inset of Fig. 1). As a result, the plasma frequency of nickel, as well as the reflection coefficient, increases: the left end of the blue arrow E indicates the maximum of the coefficient $\Delta R(t)/R_0$ due to the increase in the nickel density in the skin layer. This is the first of three distinct maxima in the time interval E. The fourth echo maximum is poorly visible due to the addition with undamped oscillations in the time interval BO. The amplitudes of the bursts associated with the echo decrease in the geometric sequence with the common ratio R_{ac}. This is associated with the end of the blue double-sided arrow E in Fig. 1.

3. ACOUSTIC DETAILS AND THE IMPOSSIBILITY OF EXPERIMENTAL OBSERVATION OF BRILLOUIN OSCILLATIONS THROUGH THE FILM IN THE CASE OF UNIFORM THICK FILMS

Our description of acoustics by means of numerical simulation is based on a two-temperature hydrodynamic code [7, 19]. The code accurately includes two-temperature and nonlinear effects; i.e., it is free from the limitations of linear acoustics. Thus, the hydrodynamic code describes the acoustic pattern of generation, propagation, reflection and passage of the wave in the film–substrate system. In this respect, the situation is equivalent to optoacoustic approaches [15, 16, 18]; except for the freedom to choose the film thickness (see below) and often disregarded details related to two-temperature effects and nonlinearity.

In our device, the nickel film is geometrically and optically (formally, in terms of the thickness of the skin layer) thick: $d_f = 70$ nm and $d_{sk} = 11.5$ nm. The transmittance of a homogeneous film in one direction is equal to $T_f = \exp(-d_f/d_{sk}) = 1/440$ [7]. The double passage of the film reduces the reflection coefficient from the acoustic wave by a factor of $440^2 = 2 \times 10^5$. Corrections Δn to the refractive index of glass, due to compression and rarefaction in the acoustic wave, are no more than 0.8% at the maximum permissible fluence $F_{max|abs} = 10.9$ mJ/cm^2. At $F > F_{max}$, the film is destroyed due to multiple repetitions required in the lock-in detection scheme. Corrections Δn are proportional to the amplitude of the acoustic wave. The calculations in [7] for glass give $\Delta n/n_0 = 0.3\Delta\rho/\rho_0$. The smallness of Δn means that the reflection from the acoustic wave is quite weak.

Even the most sensitive system for measuring the reflection coefficient $R(t)$ cannot currently detect such negligible variations of R. Therefore, to increase the film transmittance T_f in conventional optoacoustics [15, 16, 18], extremely thin films with the thickness $d_f \sim d_{sk}$ are used (in metals, $d_{sk} \sim 10$ nm), e.g., Al films with a thickness of $d_f = 10$–20 nm [15, 18]; Cr films with $d_f = 10$–14 nm [17, 20]; Pt film with $d_f = 5$ nm [21]; Ti films with $d_f = 12$–25 nm [22]; Au films with $d_f = 10$–20 nm [23]; and Ru films with $d_f = 1.2$–20 nm [24]. Alternatively, in the case of thick films, BOs are observed from the side of the transparent substrate. Sometimes, only the processes in the film are analyzed (echo analysis, time interval E in Fig. 1) [7, 19, 25, 26]. In contrast to the above-mentioned "ordinary" films, our meta-nanofilms transmit light, although geometrically they are thick in terms of the skin layer, see below discussion of extraordinary transmittance and spacing between bursts in an acoustic wave.

As mentioned above, the thickness of the zigzag "triangles" in the inset of Fig. 1 is determined by the heating layer with the thickness $d_T > d_{sk}$. Therefore, the

films in the above-mentioned "ultrathin" modes with $d_f \sim d_{sk}$ are heated by a femtosecond pulse in a supersonic manner approximately uniformly and then oscillate as a whole [27]. In our case, the thickness $d_T \approx 25$ nm is several times less than the thickness of the film $d_f = 70$ nm. Correspondingly, the acoustic wave in our case runs between the edges fr and cb of the film and, importantly, unlike the case $d_f \sim d_{sk}$, has a spatially narrow region of abrupt change of sign between the red circle and the blue diamond in the inset of Fig. 1. This is the key difference of our optoacoustic case with $d_f \gg d_{sk}$ from the usual optoacoustic case with $d_f \sim d_{sk}$.

For estimates, let us assume that the speeds of sound in the film, $c_{s|f}$, and the substrate, $c_{s|gl}$, are approximately the same. In this case, the thickness of the zigzag triangles in the substrate is the same as in the film $d_T \approx 25$ nm. In this case, the distance between the bursts (narrow regions of sign change) in the wave in the substrate is specified by the expression

$$d_{ac} = \left(2d_f/c_{s|f}\right)c_{s|gl} \approx 2d_f, \quad (1)$$

which gives the value $d_{ac} \approx 140$ nm. Thus, by increasing the value d_f in Eq. (1), we extend the bursts by an increased distance d_{ac}. As seen, the acoustic wave is characterized by two independent scales d_T and d_{ac}.

Brillouin oscillations have the resonant length

$$d_{res} = \lambda/(2n_0), \quad (2)$$

where λ is the wavelength of the probe pulse and n_0 is the unperturbed refractive index of the glass. Under our conditions, $d_{res} \approx 270$ nm. The period of BOs is related to the resonant length as

$$T_{BO} = d_{res}/c_{s|gl}. \quad (3)$$

Under our conditions, $T_{BO} \approx 50$ ps. This is the period of BOs in the time interval BO in Fig. 1. The resonant length (2) and the period (3) are due to interference associated with "mirrors" of the film and the acoustic wave in the glass.

An interesting question is what will change if the selection of the thickness of the metafilm d_f ensures the Bragg-type condition (at long times, the bursts form a long chain)

$$d_{ac} = d_{res}. \quad (4)$$

Here, the left and right sides are given by Eqs. (1) and (2), respectively. The bursts are due to successive arrivals of the steep section between the red circle and the blue diamond in the inset of Fig. 1 at the contact cb. The form of the chain is shown in Fig. 2 and in other figures. Thus, the Bragg resonance is achieved when the distance between the acoustic bursts given by Eq. (1) is equal to the period specified by Eq. (2). The change in the amplitude and phase of the BOs near the critical condition (4) will be considered in the future.

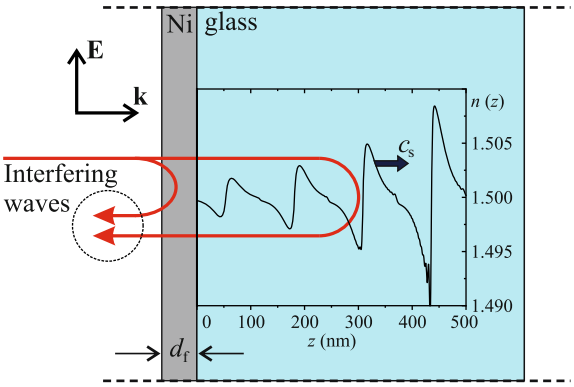

Fig. 2. (Color online) Schematic representation of the studied geometry simulated by the T-matrix method. The red lines with arrows schematically show the radial trajectories of the interfering beams that generate Brillouin oscillations.

Here, we only analyze the phase of BOs beyond the condition (4).

4. PHASE OF ACOUSTIC OSCILLATIONS IN THE EXPERIMENT

In classical nanophotonics [1–5], metasurfaces remaining stationary transform photon fluxes. Correspondingly, the period of BOs T_{BO} given by Eq. (3) and acoustic phases are meaningless, because deformations variable in time, as well as BOs, are absent. In conventional optoacoustics, ultrathin metal films with the width $d_f \sim d_{sk} \sim 10$ nm $\ll \lambda$ on dielectric or semiconductor substrates are used. To the best of our knowledge, the phase shift of BOs has not yet been analyzed in such optoacoustic experiments with probe pulses incident on the front side (i.e., through the film).

The time dependence of the correction $\Delta R(t)/R_0$ to the reflection coefficient is approximately periodic (see the interval BO in Fig. 1). Let us approximate this dependence by a single cosine:

$$f(t) = A\cos\left(\frac{2\pi}{T_{BO}}(t-\psi)\right) + \Delta f(t). \quad (5)$$

Time is measured from the maximum intensity of the pump pulse, which is a laser pulse with a duration of 150 fs [19]. This duration is extremely short compared to optoacoustic time scales. Therefore, we will assume that the system is instantaneously initiated at the time $t = 0$. Time on the abscissa axis in Fig. 1 and in Eq. (5) is measured from this point. The speed of light is five orders of magnitude higher than the speed of an acoustic wave. Accordingly, during the diagnosis of the probe pulse, the Doppler effect can be neglected and the refractive index disturbance in the acoustic wave can be considered stationary.

An important component in Eq. (5) is a smooth addition $\Delta f(t)$. This is an addition to the dependence $\Delta R(t)/R_0$ after subtracting the oscillating contribution. The function $\Delta R(t)/R_0$ approaches zero (i.e., the green dashed horizontal straight line in Fig. 1) due to the cooling of the nickel film. This is the basis for the latest measurements of the thermal conductivity [17, 28, 29] and even diffusion at the nanoscale. In this case, thick films can be used, because the measurement of the oscillating component is not necessary. Optoacoustic measurements of the diffusion of drugs in living tissues are of exceptional importance for biomedicine [30, 31]. The analysis of the smooth function $\Delta f(t)$ in our experiment requires a separate investigation.

In this work, we approximate the oscillating component in the time dependence $\Delta R(t)/R_0$ in the third time interval BO in Fig. 1. The phase ψ, as well as the time t, in Eq. (5) is measured in picoseconds. This phase in radians is given by the formula

$$\psi_{\text{rad}} = \frac{2\pi}{T_{\text{BO}}}\psi.$$

The dependence of the variable thermoreflectance $\Delta R(t)/R_0$ in the time interval BO is shown in Fig. 1. To determine the period and phase of BOs, this dependence was approximated in two ways. In the first method, we neglected the smooth component $\Delta f(t)$ in Eq. (5). In the second method, the component $\Delta f(t)$ in the time interval of experimental measurements up to 300 ps was approximated by the linear function

$$\Delta f(t) = y_0 + Bt \quad \text{with} \quad y_0 = -0.00203$$
$$\text{and} \quad B = 1.81\times10^{-6},$$

where t is the time in picosecond, so that $\Delta f(t = 300\ \text{ps}) - y_0 = 0.000543$; i.e., $\Delta f(t = 300\ \text{ps}) = -0.00149$.

The period T_{BO} in the first and second approximations is 47.5 and 46.8 ps, respectively. The phase ψ in the first and second approximations turned out to be 6.1 ps ($\psi/T_{\text{BO}} = 0.13$) and -2.75 ps ($\psi/T_{\text{BO}} = -0.06$), respectively.

Thus, the phase ψ in our experiment is approximately zero within the accuracy of the approximations.

5. SIMULATION OF BRILLOUIN OSCILLATIONS BY THE TRANSFER MATRIX METHOD

We consider a model system consisting of the nickel film, glass substrate, and an acoustic wave in the glass substrate, illuminated by a probe electromagnetic plane wave normally incident from the film side (see Fig. 2). The transfer matrix (T-matrix) method, which is used in this preliminary stage of simulation, is designed for layered media and requires spatial invariance of the simulated structure in the transverse directions. For this reason, we approximate the real nanostructured film with a homogeneous nickel film with a thickness of $d_{\text{f}} = 24$ nm, at which its transmittance corresponds to the experimentally measured transmittance of the nanostructured film ($\approx$7% at $\lambda = 793$ nm).

The acoustic wave generated by the nickel film induces a variation $\Delta n = n - n_0$ of the refractive index in it in the form of a chain of bursts and triangles in Fig. 2. The origin of the bursts was explained in Sections 2 and 3, see the inset of Fig. 1 and the discussion of the independence of the sizes of the triangles d_T and the intervals between bursts d_{ac} (1). The acoustic wave travels through the glass at the speed of sound in the glass ($c_{\text{s|gl}} = 5.57$ nm/ps).

In the T-matrix calculation, the variation of the refractive index n is approximated by a histogram corresponding to set of layers with a constant n value within each layer. The discretization step $h = 1$ nm was chosen such that it does not affect the simulation results.

The simulation of the reflection of the probe electromagnetic wave from the moving acoustic wave was carried out in two stages. In the first stage, a transient process is simulated, during which the acoustic wave is gradually formed by an echo acting inside the nickel film. In this case, the acoustic wave gradually "exits" from the nickel film (see inset (1) of Fig. 3). The transient process ends when the entire wave leaves the nickel film. As mentioned in Sections 2 and 3, the amplitudes of bursts decrease according to a geometric sequence. Therefore, we break the chain of acoustic bursts with a length of $\approx$500 nm, which is formed in the time $\approx 500\ \text{nm}/c_{\text{s|gl}} \approx 90$ ps.

In the second step, further propagation of the acoustic wave in the glass is simulated by moving the fixed distribution of the refractive index $n(x_{\text{gl}} - c_{\text{s|gl}}t)$ in the glass by adding an additional layer with an unperturbed refractive index $n_0 = 1.5$ between the nickel film and the chain of bursts. The right edge of this layer of bursts (back edge of the chain of bursts) at a time of 250 ps is marked by the vertical dashed straight line in inset (2) of Fig. 3.

For each value of the layer thickness between the film and the trailing boundary of the chain (the gap between the mirrors), the reflection coefficient from the entire model structure is calculated. The wavelength of the probe pulse is 793 nm. According to the CRC reference data, the complex refractive index of nickel at this wavelength at room temperature is $2.47 + 4.37i$.

According to Fig. 3, the time dependence of BOs obtained in the T-matrix calculation (red line) is inconsistent (in the opposite phase) with the experiment (black line). However, as we can see, the calculated and experimental results for the period and amplitude of BOs are in good agreement. It was required to correct the zero average level of the red

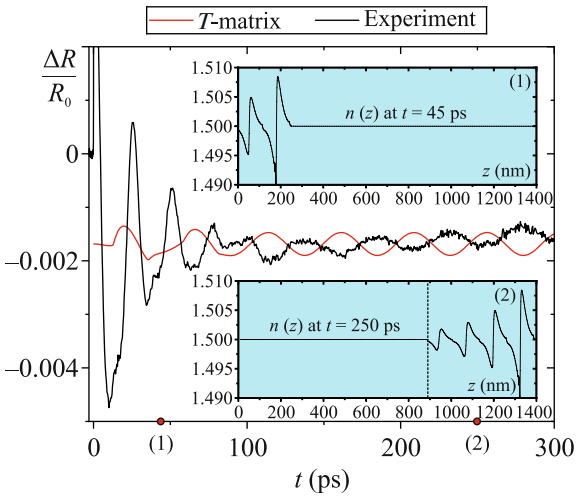

Fig. 3. (Color online) Results of simulation of Brillouin oscillations using the T-matrix. The red and black lines show the time dependences of the calculated and experimental thermoreflectance $\Delta R(t)/R_0$, respectively. To superimpose the calculated and experimental dependences, the calculated line is shifted down by 0.0017. Insets (1) and (2) show the instantaneous distributions of the refractive index of glass at times of 45 and 250 ps (marked by red circles on the time axis).

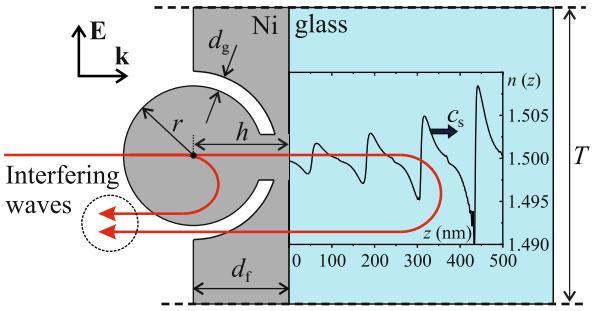

Fig. 4. (Color online) Schematic representation and parameters of the studied geometry simulated by the finite-difference time-domain method. The red lines with arrows schematically show the radial trajectories of the interfering beams that generate Brillouin oscillations. Trajectories have a conditional meaning, because reflection increases gradually on a distributed profile of a changing refractive index; i.e., there is no fixed turning point.

curve by –0.0017, because the temperature change in the complex refractive index of nickel heated above 300 K in our experiments was disregarded in the calculations performed with the refractive index at room temperature taken from CRC.

A phase shift of ≈180° is due to the limitations of the T-matrix computational model. Since the real thick nanostructured nickel film was approximated by the thin continuous homogeneous film with the same energy transmittance, we lose information on the actual phases of the interfering waves. The correct inclusion of these phases requires a more realistic model completely taking into account the nanostructure of the nickel film. this model is considered below.

6. FINITE-DIFFERENCE TIME-DOMAIN SIMULATION OF BRILLOUIN OSCILLATIONS

A real nanostructured nickel film with nanoantennas in the form of subwavelength spherical inclusions embedded in a film with a hollow gap is schematically represented in Fig. 4. As in the previous case, the film is illuminated with a normally incident plane wave and the time dependence of its reflection coefficient at a fixed wavelength of 793 nm was recorded as the acoustically induced wave propagated deep into the glass substrate.

As can be seen, the real nickel film is not spatially invariant in the transverse directions and cannot be simulated by the T-matrix method. Therefore, we performed finite-difference time-domain (FDTD) numerical simulation. The main difficulty in applying this method to simulation of the real film is that the spherical inclusions in it are distributed chaotically and do not form a regular array. However, we used a simplified approach and model a single unit cell of the array with periodic boundary conditions. Thus, the real irregular array of nanoantennas was approximated by the ideal regular array.

Such an approximation is justified for three reasons. First, nanoantennas are located in the same plane, perpendicular to the incident wave, so their random distribution in this plane does not destroy the in-phase character of the elementary waves scattered by each of them forward and backward. Chaotic background scattering at large angles to the wave vector of the incident wave, which occurs due to the disordered arrangement of inclusions on the film, is considered weak and is neglected. Second, at such periods of the array that correspond to the typical distances between inclusions in the real film (120–200 nm), there are no collective resonances in the ordered array (in the near-infrared range) due to its strict periodicity. On the other hand, nanoantennas are not very close to each other, and the radiative coupling between them, which could modify the optical response of an ordered array compared to a disordered one, can be neglected. Third, the results of the FDTD simulation even in the approximation of the ordered array already agree quite well with the experiment, as will be shown below.

In the longitudinal directions, the array unit cell was bounded by perfectly matched layers (PMLs) to absorb the transmitted and reflected waves. For an FDTD grid with rectangular cells to adequately resolve the spherical surface of the nanoantennas and the adjacent hollow gap, the mesh near a nanoantenna was locally divided. The results of FDTD simulation are presented in Fig. 5.

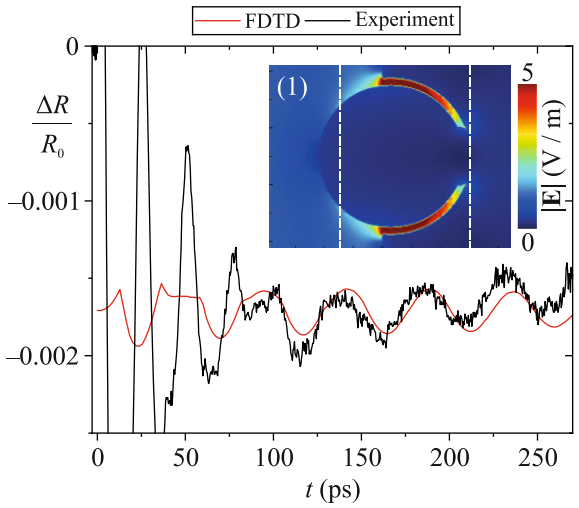

Fig. 5. (Color online) Results of finite-difference time-domain simulation of Brillouin oscillations generated by the incident electromagnetic wave with an amplitude of 1 V/m with the parameters $T = 130$ nm, $r = 50$ nm, $h = 54$ nm, $d_f = 60$ nm, and $d_g = 5$ nm (see Fig. 4). The red and black lines show the time dependences of the calculated and experimental thermoreflectance $\Delta R(t)/R_0$, respectively. Inset (1) shows the distribution of the amplitude of the electric field near the spherical inclusion. The near field is significantly amplified in the gap, as discussed in [7, 14]. The dashed vertical lines indicate the effective phase thickness of the structured nickel film (90 nm).

As can be seen in Fig. 5, the FDTD model, as well as the T-matrix model, correctly describes only the steady BOs that are observed after the completion of the transient process ($t > 90$ ps). In this case, the theoretical and experimental results for the period, amplitude, and, most importantly, the phase of oscillations are in good agreement with each other. As in the T-matrix model, the average level of the calculated relationship is shifted by –0.0017.

The comparison of the results of simulation of the smooth (see Fig. 3) and structured (see Fig. 5) films with the same transmittance indicates that the structure of the film strongly affects the phase of BOs. This is the main result of this work. In other words, the phase of BOs carries certain information on the structure of the film, because BOs in reflected light represent a signal of two-beam interference. Its result depends, first, on the phase of the wave reflected from the structured film, and, second, on the additional phase of the second wave, which passes through the film twice—before and after the reflection from the acoustic wave (see Fig. 4).

To extract useful information from the BO phase, we mentally replace the structured film with a smooth homogeneous nickel film and select its thickness in such a way that BOs from it would coincide in phase with BOs from the structured film. The effective phase thickness of the structured film obtained in this way is the information that is carried in the phase of BOs.

However, the changes in the distribution of the perturbed refractive index in the acoustic wave, which inevitably occur when the thickness of the film changes, are disregarded in this approach. Therefore, the effective film thickness obtained using this approach is, strictly speaking, an approximate estimate. However, the results of the calculations (which cannot be given here due to the limitations on the volume of this work) show that the influence of a particular profile $n(z)$ in the acoustically induced grating of the refractive index (in particular, its period) on the phase of the wave reflected from it and on the phase of the resulting BOs is very weak in our case. Therefore, the estimate obtained in this way has a fairly high accuracy.

Let us explain the proposed approach using the examples considered above. Fitting the calculated dependences in Figs. 3 and 5 by sinusoids, we determine the exact difference between their initial phases, which turns out to be equal to 2.598 rad.

Further, it should be noted that with an increase in the thickness of the continuous nickel film from d_f to d_f', the phase difference between the interfering beams, which determines the phase of the signal of BOs will change only due to the double phase increase in the electromagnetic wave in nickel on the difference in distances $d_f' - d_f$, namely, by

$$(2 \times 2\pi/\lambda)(d_f' - d_f)\mathrm{Re}(n_{Ni}).$$

Equating this expression to 2.598, we find $d_f' \approx 90$ nm, which is indicated by the vertical dashed straight lines in the inset of Fig. 5. A smooth nickel film of this thickness would give a signal of BOs that coincides in phase with the signal of BOs from the real nanostructured film.

Once again, we emphasize that the above considerations do not accurately describe the real physical situation with the thick continuous nickel film. In reality, the use of such a thick film, first, would change the form of the acoustic wave in the glass substrate, which could affect the phase of one of the interfering waves and, accordingly, the phase of BOs. Second, the energy transmittance of such a thick continuous nickel film is so small that it is impossible to observe BOs through it in practice.

7. CONCLUSIONS

Brillouin scattering in a glass substrate with a metal metamaterial film with an irregular arrangement of structures, which is used as an optoacoustic transducer, has been comprehensively analyzed.

Numerical simulation with a hybrid approach that combines hydrodynamic analysis with electrodynamic T-matrix and finite-difference time-domain simula-

tions has been performed for the first time. It has been shown for the first time that the phase of Brillouin oscillations is associated with the morphology of our nanometafilm, i.e., with spatial heterogeneity created by chaotically located elements (meta-atoms, nanoantennas).

This allows one to extract information on the morphology of the metafilm from the measurements of the metafilm transmittance and the phase of Brillouin oscillations in the substrate, namely, to approximately determine its effective phase thickness. This greatly simplifies the diagnosis of nanomaterials, compared to complex and expensive methods (focused ion beam, scanning electron microscopy, transmission electron microscopy).

ACKNOWLEDGMENTS

The equipment of the Center for Collective Use "Laser Femtosecond Complex," Joint Institute for High Temperatures, Russian Academy of Sciences was used.

FUNDING

This work was supported by the Russian Science Foundation (project no. 24-19-00311, experiments), by the Ministry of Science an Higher Education of the Russian Federation (state assignment no. FFWR-2024-0013 of the Landau Institute for Theoretical Physics, Russian Academy of Sciences and the state assignment no. FWFW-2026-0006 of the Institute of Automation and Control Processes, Far Eastern Branch, of the Russian Academy of Sciences, the theory and simulation).

CONFLICT OF INTEREST

The authors of this work declare that they have no conflicts of interest.

REFERENCES

1. Y. Liu and X. Zhang, "Metamaterials: A new frontier of science and technology," Chem. Soc. Rev. **40**, 2494 (2011).
2. N. I. Zheludev and Y. S. Kivshar, "From metamaterials to metadevices," Nat. Mater. **11**, 917 (2012).
3. A. Kuchmizhak, O. Vitrik, Yu. Kulchin, D. Storozhenko, A. Mayor, A. Mirochnik, S. Makarov, V. Milichko, S. Kudryashov, V. Zhakhovsky, and N. Inogamov, "Laser printing of resonant plasmonic nanovoids," Nanoscale **8**, 12352 (2016).
4. S. A. Syubaev, A. Y. Zhizhchenko, D. V. Pavlov, S. O. Gurbatov, E. V. Pustovalov, A. P. Porfirev, S. N. Khonina, S. A. Kulinich, J. B. B. Rayappan, S. I. Kudryashov, and A. A. Kuchmizhak, "Plasmonic nanolenses produced by cylindrical vector beam printing for sensing applications," Sci. Rep. **9**, 19750, (2019)
5. D. V. Pavlov, A. B. Cherepakhin, A. Y. Zhizhchenko, A. A. Sergeev, E. V. Mitsai, A. A. Kuchmizhak, and S. I. Kudryashov, "Third-harmonic generation in plasmonic metasurfaces fabricated by direct femtosecond laser printing," JETP Lett. **119**, 763 (2024)].
6. A. I. Aristov, U. Zywietz, A. B. Evlyukhin, C. Reinhardt, B. N. Chichkov, and A. V. Kabashin, "Laser-ablative engineering of phase singularities in plasmonic metamaterial arrays for biosensing applications," Appl. Phys. Lett. **104**, 2014 (2014).
7. Yu. V. Petrov, S. A. Romashevskii, A. V. Dyshlyuk, V. A. Khokhlov, E. M. Eganova, M. V. Polyakov, S. A. Evlashin, S. I. Ashitkov, O. B. Vitrik, and N. A. Inogamov, "Anomalous light transmission of optically thick nickel films acting as optoacoustic transducers," Zh. Eksp. Teor. Fiz. **167**, 645 (2025).
8. Ph. Lalanne, M. Chen, C. Rockstuhl, A. Sprafke, A. Dmitriev, and K. Vynck, "Disordered optical metasurfaces: Basics, properties, and applications," Adv. Opt. Photon. **17**, 45 (2025).
9. N. A. Inogamov, V. V. Zhakhovsky, S. I. Ashitkov, et al., "Surface nanodeformations caused by ultrashort laser pulse," Eng. Failure Anal. **47**, 328 (2015).
10. A. A. Ionin, S. I. Kudryashov, S. V. Makarov, A. O. Levchenko, A. A. Rudenko, I. N. Saraeva, D. A. Zayarny, C. R. Nathala, and W. Husinsky, "Nanoscale surface boiling in sub-threshold damage and above-threshold spallation of bulk aluminum and gold by single femtosecond laser pulses," Laser Phys. Lett. **13**, 025603 (2016).
11. A. Y. Vorobyev and Ch. Guo, "Enhanced absorptance of gold following multipulse femtosecond laser ablation," Phys. Rev. B **72**, 195422 (2005).
12. S. I. Kudryashov, "Ablative modification of graphite surfaces by single intense femtosecond pulses," J. Appl. Phys. **100**, 036103 (2006).
13. A. Ya. Vorobyev and C. Guo, "Colorizing metals with femtosecond laser pulses," Appl. Phys. Lett. **92**, 041914 (2008).
14. A. V. Dyshlyuk, N. A. Inogamov, and O. B. Vitrik, "Optical properties of the substrate-buried spherical dipole nanoantenna," Bull. Russ. Acad. Sci.: Phys. **88**, S450 (2024).
15. A. Devos, R. Cote, G. Caruyer, and A. Lefevre, "A different way of performing picosecond ultrasonic measurements in thin transparent films based on laser-wavelength effects," Appl. Phys. Lett. **86**, 211903 (2005).
16. V. E. Gusev and P. Ruello, "Advances in applications of time-domain Brillouin scattering for nanoscale imaging," Appl. Phys. Rev. **5**, 031101 (2018).
17. X. Tu, Y. Zeng, Sh. Wang, L. Li, Ch. Li, and Zh. Wang, "Comprehensive characterization of thermal and mechanical properties in thin metal film–glass substrate system by ultrafast laser pump–probe method," Opt. Express **30**, 46193 (2022).
18. E. Zhang, H. Zhao, Zh. Geng, X. Yan, X. Xu, and J. Dai, "Influence of layer thickness on time domain Brillouin scattering oscillation amplitude in multilayer films," J. Appl. Phys. **136**, 225302 (2024).
19. V. A. Khokhlov, S. A. Romashevskiy, S. I. Ashitkov, and N. A. Inogamov, "Synchronous detection of nonlinear phenomena in opto-acoustic vibrations induced in a nanofilm by a femtosecond laser pulse," JETP Lett. **120**, 531 (2024).

20. A. Levchuk, B. Wilk, G. Vaudel, F. Labbé, B. Arnaud, K. Balin, J. Szade, P. Ruello, and V. Juvé, "Coherent acoustic phonons generated by ultrashort terahertz pulses in nanofilms of metals and topological insulators," Phys. Rev. B **101**, 180102 (2020).
21. K. E. O'Hara, X. Hu, and D. G. Cahill, "Characterization of nanostructured metal films by picosecond acoustics and interferometry," J. Appl. Phys. **90**, 4852 (2001).
22. E. Tzianaki, M. Bakarezos, G. D. Tsibidis, Y. Orphanos, P. A. Loukakos, C. Kosmidis, P. Patsalas, M. Tatarakis, and N. A. Papadogiannis, "High acoustic strains in Si through ultrafast laser excitation of Ti thin-film transducers," Opt. Express **23**, 17191 (2015).
23. K. Yu, T. Devkota, G. Beane, G. P. Wang, and G. V. Hartland, "Brillouin oscillations from single Au nanoplate opto-acoustic transducers," ACS Nano **11**, 8064 (2017).
24. G. de Haan, T. J. van den Hooven, and P. C. M. Planken, "Ultrafast laser-induced strain waves in thin ruthenium layers," Opt. Express **29**, 32051 (2021).
25. E. A. Danilov and S. A. Uryupin, "Generation and detection of sound at the effect of femtosecond pulses on a metal film on a dielectric substrate," J. Appl. Phys. **133**, 203101 (2023).
26. E. A. Danilov and S. A. Uryupin, "Influence of inhomogeneous temperature and field distribution on sound generation and its effect on reflectivity of a thin film heated by a femtosecond pulse," J. Appl. Phys. **136**, 015304 (2024).
27. N. A. Inogamov, V. V. Zhakhovskii, and V. A. Khokhlov, "Jet formation in spallation of metal film from substrate under action of femtosecond laser pulse," J. Exp. Theor. Phys. **120**, 15 (2015).
28. W. Ma, T. Miao, X. Zhang, M. Kohno, and Y. Takata, "Comprehensive study of thermal transport and coherent acoustic-phonon wave propagation in thin metal film–substrate by applying picosecond laser pump–probe method," J. Phys. Chem. C **119**, 5152 (2015).
29. T. Miao, W. Ma, Sh. Yan, X. Zhang, M. Kohno, Y. Takata, and Y. Ikoma, "Thermal transport and thermal stress in a molybdenum film–glass substrate system", J. Vac. Sci. Technol. B **34**, 021801 (2016).
30. Ch. Wu, V. Yu. Zaitsev, and L. V. Zhigilei, "Mechanism of acoustically induced diffusional structuring of surface adatoms," Appl. Phys. Lett. **103**, 221601 (2013).
31. A. A. Selifonov and V. V. Tuchin, "Determination of the diffusion coefficient of 40%-glucose in human gum tissue by optical method," Opt. Spectrosc. **128**, 766 (2020).

Translated by R. Tyapaev